Journal of
Materials Chemistry A

Materials for energy and sustainability

Accepted Manuscript

This article can be cited before page numbers have been issued, to do this please use: X. Lin, S. Xu, Z. Wei, S. Hou, Q. Mo, X. Fu and F. Xiao, *J. Mater. Chem. A*, 2020, DOI: 10.1039/D0TA07235D.

ROYAL SOCIETY OF CHEMISTRY

rsc.li/materials-a

View Article Online
DOI: 10.1039/D0TA07235D

Journal Name

ARTICLE

Selective Organic Transformation Over Self-Assembled All-Solid-State Z-scheme Core-Shell Photoredox System

Xin Lin, Shuai Xu, Zhi-Quan Wei, Shuo Hou, Qiao-Ling Mo, Xiao-Yan Fu, Fang-Xing Xiao*

Received 00th January 20xx,
Accepted 00th January 20xx

DOI: 10.1039/x0xx00000x

www.rsc.org/

Z-scheme artificial photosystems, resembling the natural photosynthesis procedure, circumvents the disadvantage of single-ingredient photosystem and holds fascinating prospect for solar energy conversion. Despite the advancements, bottom-up elaborate design of composite heterostructured Z-scheme photosystems by flexible interface engineering for photoredox organic transformation has been poorly investigated. We herein report the construction of metal-based Z-scheme photoredox system via a progressive self-assembly strategy integrated with a facile photo-deposition. Tailor-made hierarchically branched ligand-capped Pd nanocrystals (NCs) sandwiched in-between WO_3 nanorods (NRs) core and CdS shell are harnessed as the charge transport modulator to regulate the interfacial oxidation-reduction kinetics for boosted Z-scheme photocatalysis. The intermediate Pd NCs as Schottky-type electron flow mediators considerably accelerates the unidirectional Z-scheme charge motion rate, endowing multilayered WO_3@Pd@CdS core-shell heterostructures with significantly boosted net efficiency of photoactivities toward anaerobic selective nitroaromatics reduction to amino derivatives and aromatic alcohols oxidation to aldehydes under visible light illumination. Predominant active species produced in the versatile photocatalytic selective organic transformation were explored and photocatalytic mechanisms were thus ascertained. Our endeavor could offer a promising route for smartly crafting diverse heterostructured Z-scheme photoredox systems for solar energy conversion.

1. Introduction

Semiconductor-based artificial photocatalysis holds a sustainable and promising prospect for solar energy conversion.[1-10] Solar conversion efficiency of photocatalysts is predominantly dominated by the following two factors: (1) bandgap (E_g) of photocatalyst should be smaller than the incident photon energy; (2) photoredox potentials of reactants should be positioned in-between the valence band (VB) and conduction band (CB) of photocatalyst.[3] It means that narrow E_g fosters light harvesting and conversion, and more negative CB or positive VB potential is thermodynamically beneficial for the photo-induced reduction and oxidation kinetics, respectively.[11] Single-component photosystem is featured by ultra-fast charge recombination rate and scarcity of active sites, which inevitably results in confined light absorption and insufficient redox potential.[12] In terms of conventional type-II photocatalytic (PC) system, photo-induced charge carriers are isolated in spatial separated two reverse direction, which effectively retards the charge recombination, but redox capabilities of electrons and holes are substantially reduced after separation.[13, 14] Z-scheme photosystems have been evidenced as a widely accepted tactic to increase the spatial charge separation and retain the redox potentials of charge carriers.[15-17] Thus, explosive Z-scheme photosystems have been developed for multifarious photocatalysis including hydrogen and oxygen evolution,[18, 19] carbon dioxide (CO_2) reduction,[20] bacteria disinfection and selective organic transformation.[21-23]

Considering the favorable bandgap and energy band structures, CdS and WO_3 have been frequently integrated to craft composite heterostructured Z-scheme photosystems.[3,24] Noteworthily, WO_3 is featured by high VB potential, chemical and thermal stability, but low CB level retards its access to photoreduction catalysis.[5] Contrarily, CdS demonstrates the favorable CB position which endows it with good photoreduction capability.[25,26] Complementary energy level alignment thus renders WO_3 and CdS suitable building blocks for constructing elegant Z-scheme photoredox systems.[27-30] Although all-semiconductor-based Z-scheme photosystems can accelerate the interfacial charge separation to some extent, fine tuning of charge recombination kinetics between the holes of CdS and electrons WO_3 by metal nanocrystals (NCs) enabled Schottky-type electron flow provides an alternative strategy to further boost the Z-scheme charge transport efficiency. Inspired by our recent work,[31] which manifests ligand-initiated self-assembly of Pd NCs on the WO_3 markedly benefits boosted photoactivities toward versatile visible-light-driven photo-oxidation reactions owing to the directional Schottky-junction-driven electron transfer caused by Pd NCs. Hence, we speculate judicious integration of Pd NCs in-between WO_3 and CdS via elaborate interface engineering could benefit the construction of elegant Z-scheme PC system by synergistically and simultaneously harnessing the high-efficiency electron-withdrawing capability of Pd NCs, high VB level of WO_3 and CB level of CdS. On the other hand, it should be particularly

College of Materials Science and Engineering, Fuzhou University, New Campus, Minhou, Fujian Province 350108, China. E-mail: fxxiao@fzu.edu.cn
Electronic Supplementary Information (ESI) available. See DOI: 10.1039/x0xx00000x

emphasized that semiconductor-based Z-scheme photoredox catalysis toward selective organic transformation has so far not yet been reported.

Herein, we have constructed all-solid-state metal-based Z-scheme core-shell heterostructure by an efficient self-assembly strategy integrated with a photo-deposition method based on elaborate interface engineering. Tailor-made oppositely charged Pd NCs and WO_3 NRs building blocks are self-assembled by finely tuning the surface charges, followed by seamless CdS encapsulation via photodeposition, which constitutes the spatially hierarchical core-shell heterostructures. The resultant WO_3 NRs@Pd@CdS heterostructures demonstrate significantly improved net efficiency of photoactivities toward selective aromatic alcohols oxidation to aldehydes and aromatic nitro compounds reduction to amino derivatives under the illumination of visible light. The intermediate Pd NCs between WO_3 core and CdS shell considerably accelerate the unidirectional interfacial charge recombination kinetic for electrons in the CB of WO_3 and holes in the VB of CdS, thereby boosting the Z-scheme charge transport efficiency. The substantial reduction-oxidation potentials of electrons for CdS and holes for WO_3 take part in the selective photoreduction and photo-oxidation reactions, respectively. In addition, primary active species in-situ formed in the photoredox catalysis were probed and photocatalytic mechanisms of WO_3 NRs@Pd@CdS heterostructures were thus presented. This work would provide a feasible avenue to construct a host of all-solid-state Z-scheme photosystems for extensive photocatalytic utilizations.

2. Experimental section

2.1. Preparation

(I) *Fabrication of WO_3 NRs.*[32] WO_3 NRs were prepared by a one-step hydrothermal treatment. Detailed information was provided in SI. (II) *Preparation of Pd@DMAP NCs.*[33] Detailed information was provided in SI. (III) *Self-assembly of WO_3 NRs@Pd heterostructures.*[31] WO_3 NRs@Pd heterostructures with different percentage of Pd were fabricated by an electrostatic self-assembly method and detailed information was provided in SI. (IV) *Preparation of WO_3 NRs@Pd@CdS core−shell heterostructures.*[34] Specifically, 40 mg of $CdCl_2 \cdot 2.5H_2O$ and 10 mg of S_8 were dispersed in 50 mL of ethanol to form a stable suspension and bubbled with N_2 for 30 min in the dark. WO_3 NRs@Pd nanocomposite was distributed in the above suspension and irradiated for different time under simulated solar light (300 W Xe arc lamp, PLS-SXE300D, Beijing Perfectlight Co. Ltd, China). The samples were rinsed with ethanol/DI H_2O and dried in a vacuum oven at 333 K.

2.2. Characterization

Zeta potentials (ξ) were probed by dynamic light scattering analysis (ZetasizerNano ZS-90). Crystal structure was determined by X-ray diffraction (XRD, Philips, Holland). Transmission electron microscopy (TEM) were collected on a FEI transmission electron microscope. Fourier transform infrared (FTIR) spectra were recorded on a TJ270-30A infrared spectrophotometer. X-ray photoelectron spectroscopy (XPS) spectra were recorded on a photoelectron spectrometer (ESCALAB 250). UV-vis diffuse reflectance spectra (DRS) (Varian Cary 500 UV-vis spectrophotometer, America) were probed by utilizing BaSO4 as the background. The morphologies were probed by field-emission scanning electron microscopy (FESEM, Carl Zeiss). Specific surface areas were determined on an automated gas sorption analyzer. Photoluminescence (PL) spectra were collected on a Varian Cary Eclipse spectrometer. Hydrogen peroxide (H_2O_2) was determined by a photometric method in which N, N-diethyl-p-phenylenediamine (DPD) was oxidized by a peroxidase (POD)-catalyzed reaction.[35] The detailed information was provided in SI.

2.3. Photoredox performances

(a) Photocatalytic reduction performances

In a typical reaction, a 300 W Xe lamp (PLS-SXE300D, Beijing Perfect Light co. LTD, China) equipped with a 420 nm cut-off filter (λ>420 nm) was used as the irradiation source. 10 mg of catalyst and 40 mg of ammonium formate ($HCOONH_4$) were added into 40 mL of 4-NA aqueous solution (5 mg·L^{-1}) in a glass reactor (80 mL). Prior to irradiation, the suspension was magnetically stirred in the dark for 0.5 h to establish the adsorption-desorption equilibrium between reactant and catalyst. After the regular time interval of 5 min, 3 mL of the solution was withdrawn, centrifuged to separate the catalyst, and then analyzed on a UV-Vis spectrophotometer (Thermal Fisher, GENESYS, 10S). The whole experiments were conducted under N_2 bubbling with a flow rate of 80 mL·min^{-1}. Photoactivity of the sample was defined by the following formula.

$$\text{Conversion}\ (\%) = \left(\frac{C_0 - C}{C_0}\right) \times 100\% \quad (1)$$

where C_0 represents the initial concentration of nitroaromatics and C is the concentration after a certain time of visible light irradiation.

(b) Selective photocatalytic oxidation of aromatic alcohols

8 mg of catalyst, 0.1 mmol alcohol, and 1.5 mL of benzotrifluoride (BTF) saturated with O_2 were added into a Pyrex glass bottle with a capacity of 10 mL. The reason for choosing BTF as solvent is because of its inertness to oxidation and high solubility for molecular oxygen.[21] After stirring for 20 min in the dark, the glass bottle was then irradiated by a 300 W Xe arc lamp (PLS-SXE300D, Beijing Perfectlight Co. Ltd, China) with a UV-CUT filter (λ>420 nm). After reaction, the suspension was centrifuged at 12000 rpm and the supernatant was analyzed by a gas chromatograph (SHIMADZU GC-2014C). Conversion and yield were determined by the following formulas.[21]

$$\text{Conversion}\ (\%) = \left(\frac{C_0 - C_{\text{alcohol}}}{C_0}\right) \times 100\% \quad (2)$$

$$\text{Yield}\ (\%) = \frac{C_{\text{aldehyde}}}{C_0} \times 100\% \quad (3)$$

$$\text{Selectivity}\ (\%) = \frac{C_{\text{aldehyde}}}{C_0 - C_{\text{alcohol}}} \times 100\% \quad (4)$$

where C_0 is the initial concentration of alcohols, $C_{alcohol}$ and $C_{aldehyde}$ are the concentrations of alcohols and aldehydes after irradiation under visible light, respectively.

2.4. Photoelectrochemical (PEC) performances

PEC results were probed on an electrochemical workstation (CHI660E, CHI Shanghai, Inc.) utilizing Na_2SO_4 (100 mL, 0.5 M, pH=6.69) as the electrolyte and Pt & Ag/AgCl as the counter and reference electrodes, respectively. The working electrodes (1 X 1 cm^2) were directly irradiated by a 300 W Xe arc lamp (PLS-SXE300D, Beijing Perfectlight Co. Ltd., China) equipped with a cut-off filter (λ>420 nm). Potentials were calibrated according to the formula below:[36, 37]

$$ERHE = EAg/AgCl + 0.059pH + 0.1976V \quad (5)$$

3. Results and discussion

Scheme 1 displays the flowchart for fabricating WO_3 NRs@Pd@CdS composite core-shell photocatalysts which were elaborately prepared by depositing Pd NCs on the WO_3 NRs substrate and then a thin CdS layer was coated on the WO_3 NRs@Pd by a photo-deposition method. Note that tailor-made Pd NCs are capped by hierarchical linker (**Fig. S1**) which endows Pd@DMAP NCs with positively charged surface (**Fig. S2b**) owing to the partial protonation of the exocyclic nitrogen atom.[38] Contrarily, WO_3 NRs is negatively charged (**Fig. S2a**). Hence, Pd@DMAP NCs can be uniformly electrostatically self-assembled on the WO_3 NRs. Subsequently, uniform CdS encapsulation on the WO_3 NRs@Pd was realized by a facile photo-deposition, which ultimately results in WO_3 NRs@Pd@CdS core-shell nano-architecture.

As displayed in **Fig. 1a**, the peaks at 13.99, 22.84, 24.35, 26.82, 28.57, 36.55, 49.82 and 55.34° are accurately indexed to the crystallographic facets of WO_3 (JCPDS: 75-2187).[39] XRD pattern of WO_3 NRs@Pd@CdS heterostructure is similar to WO_3 NRs and no CdS peaks and Pd NCs are observed, which is attributed to the low deposition amount of CdS and Pd NCs relative to WO_3 NRs substrate. As displayed in **Fig. 1b** and **Table S1**, the peaks positioned at 3447.50 and 1619.24 cm^{-1} are attributed to the stretching and deformation vibration modes of surface hydroxyl (–OH) group.[37] The peaks at 2924.31 and 2834.52 cm^{-1} in the FTIR spectra of WO_3 NRs@Pd (**Fig. 1bIII**) correspond to the stretching vibration fashion of CH_2 group from DMAP ligands.[22] Peak intensity of -NH deformation vibration at 1612.84 cm^{-1} in the FTIR spectra of WO_3 NRs@Pd and WO_3 NRs@Pd@CdS [**Fig. 1b(I & III)**] is much stronger than those of WO_3 NRs@CdS and WO_3 NRs [**Fig. 1b(II & IV)**], which reflects attachment of DMAP ligand on the WO_3 NRs.[40] The peak at 824.51 cm^{-1} corresponds to the W–O group from WO_3 NRs substrate.[23] Hence, FTIR results indicate Pd@DMAP NCs have been grafted on the WO_3 NRs. Furthermore, blue-shifts of the peaks are visualized for WO_3 NRs@Pd relative to WO_3 NRs, implying electronic interaction between metal (Pd NCs) and semiconductor (WO_3 NRs). No typical CdS peak is seen in the FTIR spectra of WO_3 NRs@Pd@CdS and WO_3 NRs@CdS, which is due to the low deposition amount of CdS layer.

Fig. 1c manifests that WO_3 NRs and WO_3 NRs@Pd exhibit substantial absorption from 200 to 465 nm, which corresponds to the intrinsic bandgap photoexcitation of WO_3. WO_3 NRs@Pd exhibits a minute red-shift of the band edge accompanied by increased intensity in the visible region (465~800 nm) relative to WO_3 NRs, which is due to the background absorption of Pd NCs. Moreover, DRS spectra of WO_3 NRs@CdS and WO_3 NRs@Pd@CdS indicate light absorption of WO_3 NRs was enhanced within the visible region when an ultra-thin CdS layer was deposited on the outermost layer with absorption band edge red-shifted to longer wavelength. Apparently, WO_3 NRs@CdS and WO_3 NRs@Pd@CdS demonstrate more improved absorption in visible domain with respect to WO_3 because of the photosensitization effect of CdS, which agrees with the sample color (**Fig. S3**). As shown in **Fig. 1d**, bandgaps of WO_3 NRs, WO_3 NRs@Pd, WO_3 NRs@CdS and WO_3 NRs@Pd@CdS are determined to be 2.64, 2.54, 2.11 and 2.02 eV, respectively.[41] The result implies that depositing Pd NCs on the WO_3 NRs does not affect the light absorption band edge of WO_3 NRs but rather enhance the intensity. Obviously, bandgap of WO_3 NRs@Pd@CdS is reduced with Pd NCs and CdS decoration,

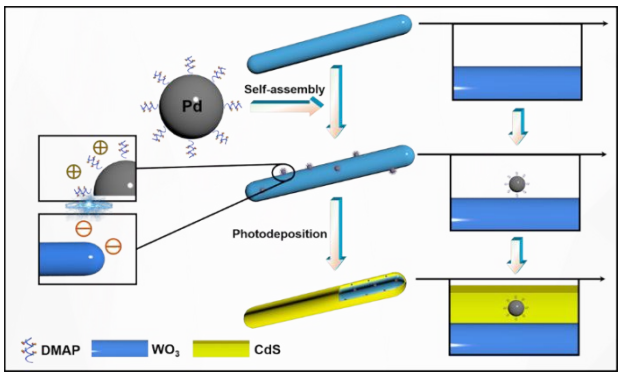

Scheme 1 Schematic demonstration for fabricating the WO_3@Pd@CdS core-shell heterostructures.

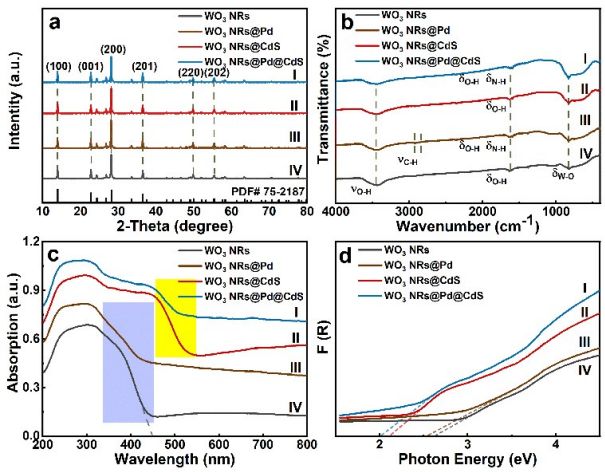

Fig. 1. (a) XRD and (b) FTIR results of (IV) WO_3 NRs, (III) WO_3 NRs@Pd, (II) WO_3 NRs@CdS and (I) WO_3 NRs@Pd@CdS; (c) DRS spectra with (d) transformed plots calculated by the Kubelka-Munk function vs. the energy of light.

which is attributed to the photosensitization of CdS for boosting light harvesting. **Fig. S4** suggests that specific surface areas and pore volumes of WO_3 NRs@Pd, WO_3 NRs@CdS and WO_3 NRs@Pd@CdS were not substantially changed relative to WO_3 NRs (**Table S2**), implying analogous adsorption capability of the samples to the reactants.[42]

As exhibited in **Fig. S5**, survey spectrum of WO_3 NRs@Pd@CdS reveals the appearance of W 4f, O 1s, Cd 3d, and S 2p signals, which verifies integration of CdS with WO_3 NRs. As displayed in the high-resolution W 4f spectrum of WO_3 NRs@Pd@CdS (**Fig. 2aII**), the peaks at 35.55 and 37.65 eV corresponds to W^{6+}, consistent with the case of WO_3 NRs (**Fig. 2aI**).[31, 43] The peak in the high-resolution O 1s spectrum of WO_3 NRs@Pd@CdS (**Fig. 2bI**) is deconvoluted to two peaks with binding energy (B.E.) of 530.5 and 532.05 eV which correspond to lattice oxygen and hydroxyl groups, respectively.[44] Similarly, B.E. of lattice oxygen for WO_3 NRs@Pd@CdS (**Fig. 2bII**) is slightly shifted relative to WO_3 NRs (**Fig. 2bI**), which implies the electronic interaction caused by Pd and CdS attachment. As reflected by the high-resolution Cd 3d spectrum of WO_3 NRs@Pd@CdS (**Fig. 2c**), the peaks at 405.2 and 411.95 eV signify the oxidation state of Cd^{2+}, which confirms the success of CdS deposition.[18, 26] As well, as reflected by **Fig. 2d**, high-resolution S 2p spectrum of WO_3 NRs@Pd@CdS demonstrates typical peaks at 162.7 and 161.45 eV which are ascribed to S^{2-}.[45, 46] **Fig. 2e** displays the high-resolution Pd 3d spectrum of WO_3 NRs@Pd@CdS, wherein the peaks at 336.5 and 341.9 eV are ascribed to metallic Pd^0.[47-50] No N signal stemming from DMAP ligand of Pd NCs was detected in the high-resolution N 1s spectrum of WO_3 NRs@Pd@CdS (**Fig. 2f & Table S3**), which is attributed to integrating Pd NCs in-between WO_3 NRs and CdS layer, shielding the peak.[51]

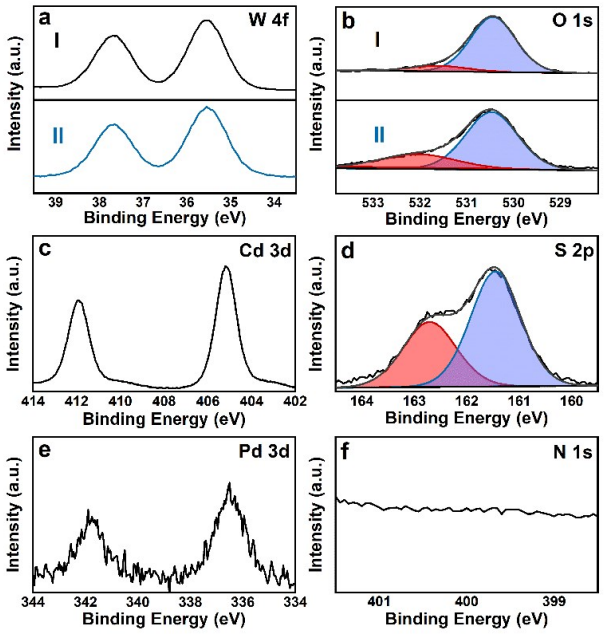

Fig. 2 High-resolution (a) W 4f, (b) O 1s spectra of (I) WO_3 NRs and (II) WO_3 NRs@Pd@CdS, and high-resolution (c) Cd 3d, (d) S 2p, (e) Pd 3d and (f) N 1s spectra of WO_3 NRs@Pd@CdS.

As visualized in **Fig. S6a**, WO_3 NRs substrate is featured by one-dimensional (1D) morphology with smooth surface. **Fig. (3a & S6b)** show that morphology of WO_3 NRs@Pd is almost the same to WO_3 NRs and this is due to the ultra-small size of Pd NCs (2.43 nm, **Fig. S1c**), making direct differentiation of Pd NCs difficult. As displayed in **Fig. (3b & S6c)** and **Fig. (3c & S6d)**, both WO_3 NRs@CdS and WO_3 NRs@Pd@CdS demonstrate rough surface which are capped with a thin CdS layer. As reflected by the TEM images of WO_3 NRs@Pd in **Fig. 3(d & e)**, WO_3 NRs possesses a size of ca. 60 nm, on which Pd NCs were attached on the surface without agglomeration. HRTEM image of WO_3 NRs@Pd (**Fig. 3f**) reveals the close integration of Pd NCs and WO_3 NRs and the lattice fringes of 0.225 and 0.389 nm are assigned to the (111) and (001) crystal facets of Pd and WO_3, respectively.[52]

TEM images of WO_3 NRs@Pd@CdS in **Fig. 3(g & h)** manifest close encapsulation of WO_3 NRs@Pd with a thin CdS layer (ca. 10-20 nm) forming the well-defined core-shell heterostructure. As exhibited in the HRTEM image (**Fig. 3i**) of WO_3 NRs@Pd@CdS, Pd NCs were intimately integrated in-between CdS layer and WO_3 and the lattice fringes of ca. 0.225, 0.338, and 0.388 nm accurately correspond to the (111), (111), and (001) crystal facets of Pd, CdS, and WO_3, respectively.[17, 52] Elemental mapping [**Fig. 3 (j-o)**] and EDS result (**Fig. S7**) corroborate the uniform distribution of W, O, Cd, S and Pd elements in the WO_3 NRs@Pd@CdS heterostructure. Moreover, increased size of the nanorods measured from element mapping results confirms deposition of Pd NCs in-between WO_3 and CdS, forming core-shell nanostructure. Consistently, as reflected by **Fig. S8**, C and N signals are from the DMAP ligand and the result corroborates the monodispersed deposition of Pd NCs in-between WO_3 NRs and CdS layer.

Photoactivities of WO_3 NRs@Pd@CdS heterostructures are probed by reduction of 4-nitroaniline (4-NA) to 4-phenylenediamine (4-PDA) under the illumination of visible light (λ>420 nm).[45] Blank experiments without adding catalyst or without light illumination (**Fig. S9**) indicate it is a photocatalytic process. As reflected in **Fig. S10**, conversion process of 4-NA to 4-PDA can be monitored by UV-vis absorption spectrum, for which the peak positioned at 380 nm corresponding to 4-NA was detected before reaction and a new peak positioned at ca. 240 nm attributable to 4-PDA gradually arises with reaction progressing, indicating photoreduction of 4-NA to 4-PDA.[46] According to our recent work,[31] optimal Pd deposition percentage of WO_3 NRs@Pd was determined as 11%. Therefore, WO_3 NRs@11Pd is utilized for fabricating WO_3 NRs@Pd@CdS heterostructures. Photoactivities of the samples are displayed in **Fig. 4a**, wherein WO_3 NRs and WO_3 NRs@11Pd exhibite negligible photoactivities, which stems from low CB potential of WO_3, making reduction of 4-NA inaccessible. Photoactivities of WO_3 NRs@Pd is remarkably improved by photo-deposition of CdS, highlighting CdS encapsulation benefits the photoactivities of WO_3 NRs@Pd@CdS, which is understandable considering the high reduction potential of CdS. Photoactivities of WO_3 NRs@Pd@CdS are substantially influenced by the photo-deposition time. To be specific, photoactivity of WO_3

View Article Online
DOI: 10.1039/D0TA07235D

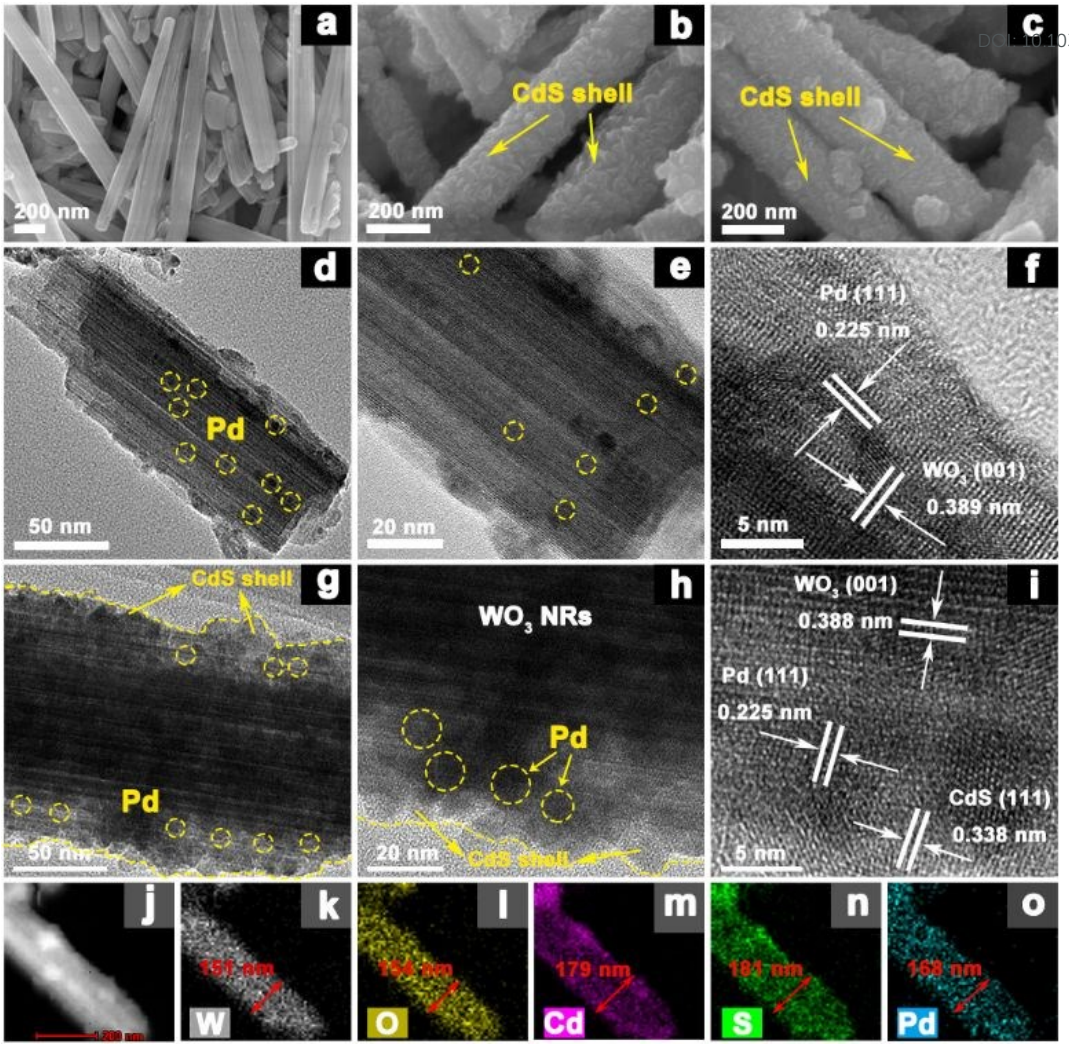

Fig. 3. FESEM images of (a) WO_3 NRs@Pd, (b) WO_3 NRs@CdS and (c) WO_3 NRs@Pd@CdS; TEM images of (d & e) WO_3 NRs@Pd with (f) HRTEM image, (g & h) TEM, (i) HRTEM and (j) STEM images of WO_3 NRs@Pd@CdS with (k-o) elemental mapping results.

NRs@Pd@CdS increases with prolonging the time to 2h and then it deteriorates when the time approaches to 5h, by which WO_3 NRs@11Pd@2CdS was determined as the optimal catalyst. Over CdS encapsulation blocks the photoexcitation of WO_3, leading to decreased photoactivity. Alternatively, over-deposited CdS layer can also cause unfavorable agglomeration which acts as the charge recombination center.

Fig. 4b shows the photoactivities of WO_3 NRs@βPd@2CdS (β=3, 5, 7, 9, 11%) heterostructures with different loading percentages of Pd NCs. The results indicate photoactivity of WO_3 NRs@βPd@2CdS increases with Pd NCs amount elevating from 3 to 7% and then it decreases with additionally increasing the percentage, among which WO_3 NRs@7Pd@2CdS demonstrate the optimal photoactivity. **Fig. 4c** shows that WO_3 NRs@7Pd@2CdS exhibits good photostability after five cyclic reactions. Consistently, XRD patterns (**Fig. S11**) of WO_3 NRs@7Pd@2CdS after cyclic reactions manifest its crystal structure was retained, confirming it is a robust and stable photocatalyst. Photoreduction of 4-NA complies with the first-order reaction kinetic, by which kinetic rate constants of the samples can thus be obtained (**Table S4**). As unveiled in **Fig. 4d**, kinetic rate constants (0.28715 min^{-1}) of WO_3 NRs@7Pd@2CdS is ca. 144 and 66 times larger than those of WO_3 NRs (0.002 min^{-1}) and WO_3 NRs@11Pd (0.00433 min^{-1}) and 4 times larger than WO_3 NRs@2CdS (0.07228 min^{-1}). The enhanced photoactivity of WO_3 NRs@7Pd@2CdS relative to WO_3 NRs@2CdS evidences the importance of Pd NCs in improving the photoactivity.

To unleash the impact of electrons in photoreduction reactions, control experiment by utilizing $K_2S_2O_8$ as electron scavenger was carried out.[25] **Fig. 4e** shows that photoactivity of WO_3 NRs@7Pd@2CdS with addition of $K_2S_2O_8$ is conspicuously reduced. Besides, photoactivity of WO_3 NRs@7Pd@2CdS with O_2 purge was considerably inferior to that under N_2 purge. The results concurrently highlight the importance of electrons in driving the reaction. As displayed in **Fig. 4f**, an obvious peak at 450 nm is visualized in the action spectrum of WO_3 NRs@7Pd@2CdS, strongly implying the pivotal role of photosensitization effect from CdS.

To unlock the general photoreduction activities of WO_3 NRs@7Pd@2CdS heterostructure, apart from 4-NA (**Fig. 5a),** a series of nitroaromatics including 3-nitroaniline (3-NA), 2-

View Article Online
DOI: 10.1039/D0TA07233D

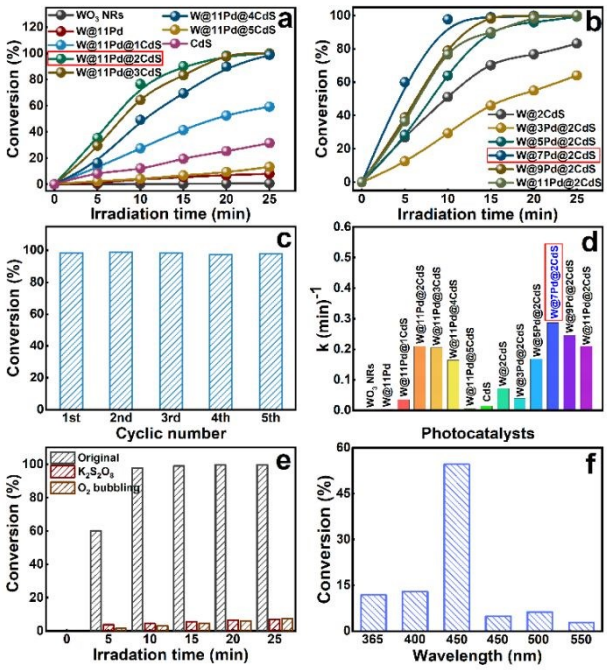

Fig. 4. (a) Photocatalytic activities of WO_3 NRs@11 wt% Pd@αh-CdS (α=1, 2, 3, 4, 5) with different photo-deposition time toward 4-NA reduction under the illumination of visible light (λ>420 nm); (b) photoactivities of WO_3 NRs@β wt% Pd@2h-CdS (β = 3, 5, 7, 9, 11) with different Pd NCs percentages under the same conditions; (c) cyclic reaction of WO_3 NRs@7Pd@2CdS and (d) apparent kinetic constants of the samples; (e) control experiments with adding $K_2S_2O_8$ in the reaction system and photoreaction performed under O_2 purge in the presence of WO_3 NRs@7Pd@2CdS; (f) photocatalytic reduction of 4-NA over WO_3 NRs@7Pd@2CdS under different monochromatic light irradiation. (WO_3 NRs@β wt% Pd@αh-CdS was abbreviated as WO_3 NRs@βPd@αCdS).

nitroaniline (2-NA), 4-nitrophenol (4-NP), 3-nitrophenol (3-NP), 2-nitrophenol (2-NP), 4-nitrotoluene (4-NT), 4-nitroanisole, nitrobenzene, *o*-nitroacetophenone, 1-chloro-4-nitrobenzene and 1-bromo-4-nitrobenzene were also utilized as the substrates for selective photoreduction catalysis. As displayed by **Fig. 5(b-l)**, analogous boosted photoactivities are visualized over WO_3 NRs@7Pd@2CdS relative to single (WO_3) and binary (WO_3 NRs@7Pd, WO_3 NRs@2CdS) counterparts under the same conditions, i.e., WO_3 NRs@7Pd@2CdS>WO_3 NRs@2CdS>WO_3 NRs@7Pd >WO_3 NRs, signifying its versatile photoactivities.

Beside the selective photoreduction catalysis, photocatalytic aromatic alcohols oxidation to aromatic aldehydes was also probed to elucidate the role of Pd NCs in promoting the interfacial charge transport. Blank experiments without catalyst or light irradiation indicate negligible conversion of alcohol (**Fig. S12**), confirming the reaction is a photocatalytic process. Detailed variation of the GC spectrum for photocatalytic selective benzyl alcohol (BA) oxidation to benzyl aldehyde (BAD) is displayed in **Fig. S13**.[21] As reflected by **Fig. 6(a-h)**, WO_3 NRs@7Pd@2CdS exhibits the optimal photoactivities toward selective oxidation of a collection of aromatic alcohols to aldehydes with high conversion and selectivity under the illumination of visible light, superior to the single (WO_3 NRs) and binary (WO_3 NRs@7Pd and WO_3 NRs@2CdS) counterparts. In contrast, WO_3 NRs shows very poor photoactivities, which is due to the ultra-short charge lifetime. Photoactivity of WO_3 NRs@7Pd is higher than WO_3 NRs to some extent, implying Pd NCs deposition can improve the photo-oxidation performance, which is because Pd NCs can serve as electron reservoirs to boost the charge separation. Moreover, considerably enhanced WO_3 NRs@2CdS relative to WO_3 NRs is observed and this corroborates the importance of CdS layer in promoting the photocatalytic activities.

As displayed in **Fig 6i**, a peak between 365 and 500 nm is observed in the action spectrum of WO_3 NRs@7Pd@2CdS toward photocatalytic selective oxidation of BA to BAD, which confirms the photosensitization effect of CdS layer on improving the photoactivities of WO_3 NRs@7Pd@2CdS. To determine the main active species participating in the selective oxidation of alcohols over WO_3 NRs@7Pd@2CdS, control experiments were performed by adding $K_2S_2O_8$, Na_2SO_3, TBA, and BQ into the reaction system to quench electron (e^-), hole (h^+), hydroxyl radical (•OH), and superoxide radical ($•O_2^-$), respectively.[53] As displayed in **Fig. 6j**, reduced photoactivity of WO_3 NRs@7Pd@2CdS was observed when Na_2SO_3, TBA, and BQ were added in the reaction system, implying h^+, •OH and $•O_2^-$ radicals all contribute to the photoactivity enhancement. Besides, photoactivity of WO_3 NRs@7Pd@2CdS was also remarkably reduced when the reaction was accessed in N_2-saturated BTF solvent, uncovering oxygen is able to reinforce the photoactivity. Notably, oxygen is indispensable to produce diverse oxygen-containing active species such as $•O_2^-$ radicals, •OH radicals and hydrogen peroxide (H_2O_2). Similar result was observed when $K_2S_2O_8$ was added into the reaction system, suggesting electron also play a crucial role in reinforcing the significantly enhanced photoactivities of WO_3 NRs@7Pd@2CdS. This is owing to the fact that electrons quenching refrains the formation of $•O_2^-$ and •OH radicals. The relationship of electrons with the $•O_2^-$, H_2O_2 and •OH formation is demonstrated by the formulas 6−8.[21] In general, influence of active species follows the order of h^+ > e^->•OH > $•O_2^-$. The variation of •OH radicals and H_2O_2 produced over different samples is verified by **Fig. (S14 & S15)**, which is in line with the photoactivities.

$$O_2 + e^- \rightarrow •O^{2-} \quad (6)$$

$$•O_2^- + •O_2^- + 2H^+ \rightarrow H_2O_2 + O_2 \quad (7)$$

$$H_2O_2 + •O_2^- \rightarrow •OH + OH^- + O_2 \quad (8)$$

Besides the photoredox catalysis in selective organic transformation, WO_3 NRs@7Pd@2CdS also demonstrates significantly improved photoactivity toward mineralization of organic pollutant (**Fig. S16**) under the illumination of visible light, implying its versatile photocatalytic performances.

Photoelectrochemical (PEC) investigations were carried out to unveil the separation efficiency of electron-hole pairs.[37, 54] **Fig. 7a** shows that photocurrent of WO_3 NRs@7Pd@2CdS is much larger than WO_3 NRs, WO_3 NRs@7Pd and WO_3 NRs@2CdS and the results agree with the photoactivities. The result indicates CdS encapsulation and Pd NCs deposition favors the charge separation of WO_3 and simultaneous Pd NCs & CdS decoration synergistically retards the charge recombination. As displayed in **Fig. 7b**, arc radius of WO_3 NRs@7Pd@2CdS is successively smaller than those of WO_3 NRs@2CdS, WO_3 NRs@7Pd and

View Article Online
DOI: 10.1039/D0TA07235D

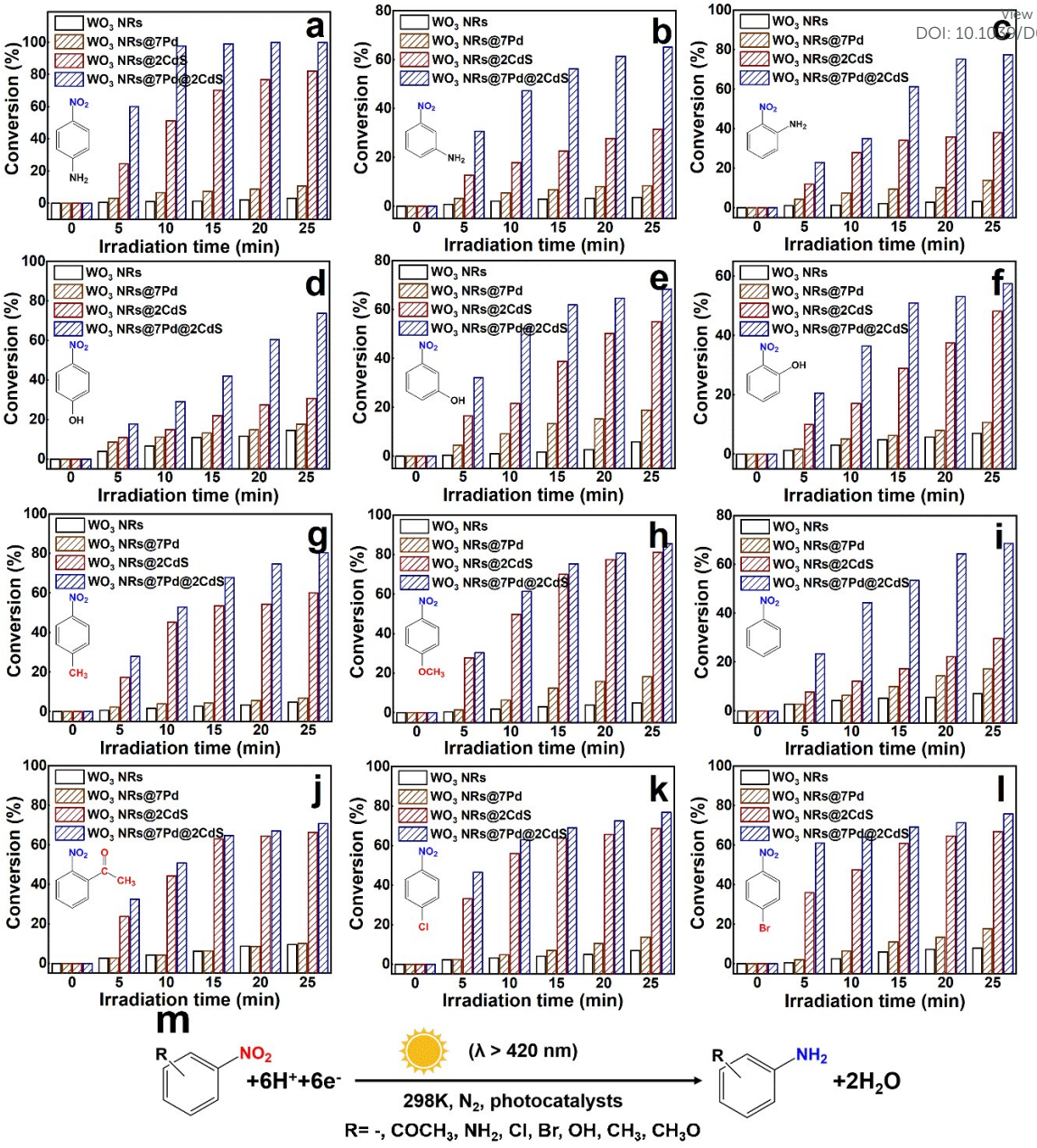

Fig. 5. (a) Photoactivities of WO_3 NRs, WO_3 NRs@7Pd, WO_3 NRs@2CdS and WO_3 NRs@7Pd@2CdS toward reduction of various nitroaromatics including (a) 4-NA, (b) 3-NA, (c) 2-NA, (d) 4-NP, (e) 3-NP, (f) 2-NP, (g) 4-nitrotoluene, (h) 4-nitroanisole, (i) nitrobenzene, (j) o-nitroacetophenone, (k) 1-chloro-4-nitrobenzene, and (l) 4-bromo-1-nitrobenzene under the illumination of visible light (λ>420 nm) with adding ammonium formate for quenching holes and N_2 bubbling along with (m) reaction model.

WO_3 NRs, which agrees with the photocurrents results (**Fig. 7a**). Among which, WO_3 NRs@7Pd@2CdS demonstrates the smallest arc radius in comparison with other counterparts, manifesting its smallest interfacial charge transfer resistance,[50] followed by WO_3 NRs@2CdS, WO_3 NRs@7Pd and WO_3 NRs, respectively. The simulated EIS results are summarized in **Table S5**, wherein WO_3 NRs@7Pd@2CdS (6529 ohm) exhibits much lower charge resistance (R_{ct}) under visible light illumination relative to the single (WO_3 NRs: 17140 ohm) and binary counterparts (WO_3 NRs@7Pd :9872 ohm; WO_3 NRs@2CdS: 7857 ohm). Mott–Schottky (M–S) results are displayed in **Fig. 7c**, by which charge densities (N_D) of the samples are estimated by the formula below:[54, 55]

$$N_D = \left(\frac{2}{e\varepsilon\varepsilon_0}\right)\left[\frac{d\left(\frac{1}{C^2}\right)}{dV}\right]^{-1} \quad (9)$$

where e=1.6 × 10^{-19} C, ε_0=8.86 × 10^{-12} F m^{-1}, ε is the dielectric constant and ε=300 for WO_3,[44] C is the capacitance. As manifested in **Fig. 7d**, N_D values of WO_3 NRs, WO_3 NRs@7Pd, WO_3 NRs@2CdS and WO_3 NRs@7Pd@2CdS are calculated as 8.83×10^{18}, 1.18×10^{19}, 1.35×10^{19} and 1.91×10^{19} cm^{-3}, respectively. N_D of WO_3 NRs@7Pd@2CdS is almost 2.2, 1.6, and 1.4 times larger than those of WO_3 NRs, WO_3 NRs@7Pd, WO_3 NRs@2CdS, consistent with other PEC results, corroborating the cooperativity of Pd NCs and CdS.

View Article Online
DOI: 10.1039/D0TA07235D

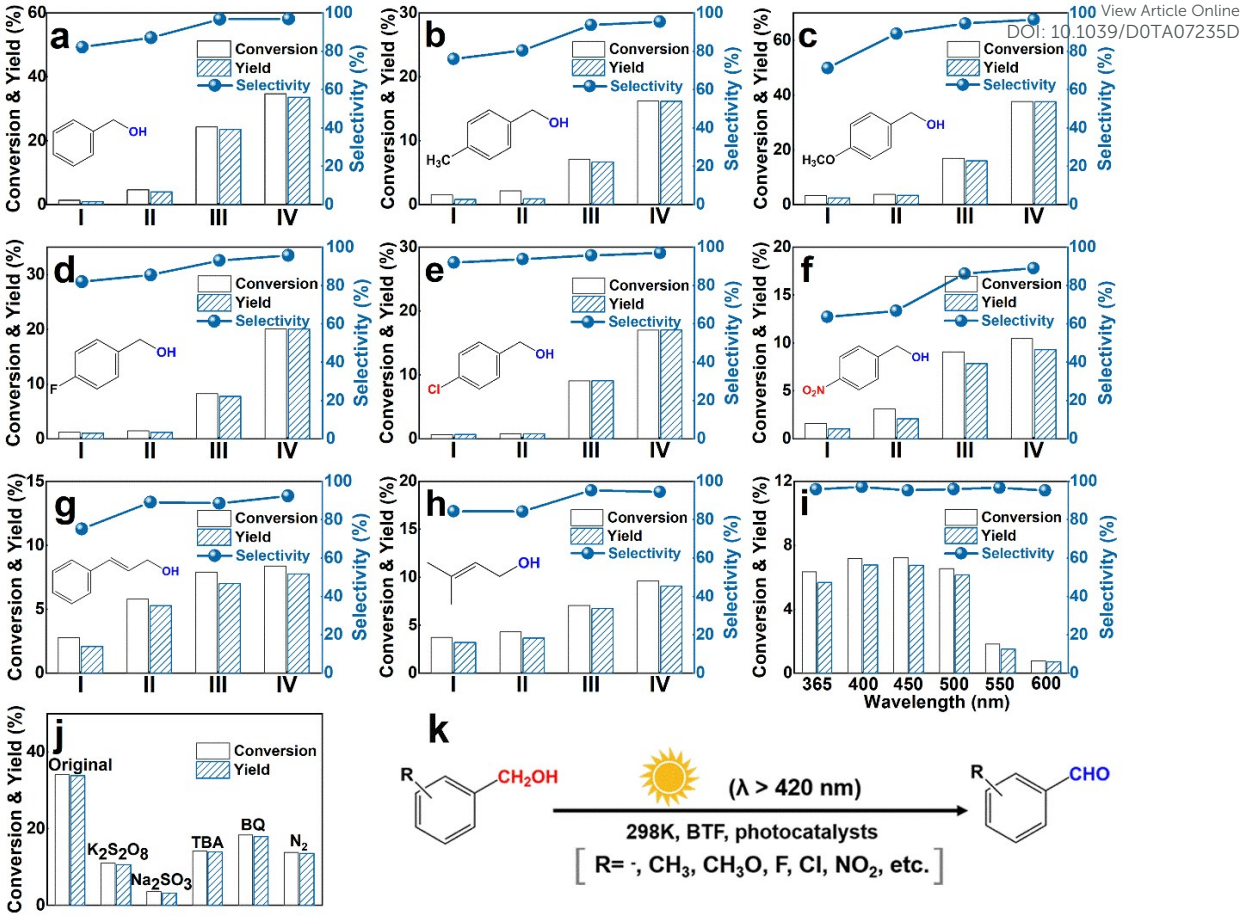

Fig. 6. Photocatalytic activities of (I) WO_3 NRs, (II) WO_3 NRs@7Pd, (III) WO_3 NRs@2CdS and (IV) WO_3 NRs@7Pd@2CdS toward selective aromatic alcohols oxidation including (a) benzyl alcohol, (b) p-methylbenzyl alcohol, (c) p-methoxybenzyl alcohol, (d) p-fluorobenzyl alcohol, (e) p-chlorobenzyl alcohol, (f) p-nitrobenzyl alcohol, (g) cinnamyl alcohol, and (h) 3-methyl-2-buten-1-ol to aldehydes under the illumination of visible light (λ>420 nm) for 4 h; (i) action spectra of WO_3 NRs@7Pd@2CdS; (j) photocatalytic selective oxidation of BA over WO_3 NRs@7Pd@2CdS with adding $K_2S_2O_8$, Na_2SO_3, TBA, and BQ for quenching electron (e^-), hole (h^+), hydroxyl radical (•OH), and superoxide radical ($•O_2^-$), and photoactivity with N_2 bubbling, along with (k) reaction model.

Photoluminescence (PL) has been deemed as an effective technique to evaluate the interfacial charge separation efficiency of semiconductor.[17, 56] As displayed in **Fig. 7(e & f)**, WO_3 NRs@7Pd demonstrates lower PL intensity than WO_3 NRs, which suggests electrons in the CB of WO_3 can be captured by Pd NCs, resulting in decreased charge recombination. PL intensity of WO_3 NRs@CdS is lower than WO_3 NRs, which is owing to the generation of type II energy band structure for enhancing charge separation. The lowest PL intensity was observed over WO_3 NRs@7Pd@2CdS, implying charge separation was additionally enhanced with simultaneous Pd NCs and CdS deposition. Note that WO_3 NRs@7Pd@2CdS shows lower PL intensity than WO_3 NRs@2CdS, once again confirming the crucial role of Pd in increasing interfacial charge separation.

Energy levels of WO_3 and CdS in the WO_3 NRs@7Pd@2CdS were probed by M-S results and VB XPS results. **Fig. S17** shows the VB spectrum of WO_3,[57] by which VB of WO_3 is determined to be 2.62 V vs. NHE. **Fig. S18** exhibits the M-S plot of CdS,[58] by which flat band potential of CdS is determined as -0.49V vs. NHE. Considering the E_g of WO_3 (2.86 eV) and CdS (2.35 eV) (**Fig. S19**), CB level of WO_3 and VB level of CdS are deduced to be -0.24 and 1.86 V vs. NHE, respectively. The possible charge transport pathways were depicted in **Fig. S20**. There are two charge transport channels for WO_3 NRs@Pd@CdS heterostructures including conventional type-II and Z-scheme photocatalytic mechanisms. Concerning the type-II charge transfer pathway (**Fig. S20a**), electrons in the CB of CdS migrate to the CB of WO_3 accelerated by Pd NCs and holes in the VB of WO_3 move to the VB of CdS, resulting in effective charge separation. However, redox potentials of electrons and holes would be considerably reduced in such charge transfer pathway, thereby rendering photoreduction of nitroaromatics inaccessible, which is inconsistent with our results. Furthermore, if such a type-II charge transport mechanism occurs, electrons in the CB of WO_3 (-0.24 V vs. NHE) fail to achieve reduction of O_2 to $•O^{2-}$ radicals due to the larger potential of $O_2/•O^{2-}$ [$E_{(O_2/•O^{2-})}$=−0.284 V vs. NHE]. Analogously, holes in the VB of CdS (+1.86 V vs. NHE) do not enable oxidation of H_2O to •OH radicals due to the larger oxidation potential of $H_2O/−OH$ [$E°_{(•OH/H_2O)}$=+2.38 V vs. NHE]. However, generation of $•O^{2-}$ and •OH radicals in our current reaction system has been undoubtedly confirmed by control experiments, eliminating the occurrence of type-II charge transfer mechanism. Hence, we believe Z-scheme charge

View Article Online
DOI: 10.1039/D0TA07255D

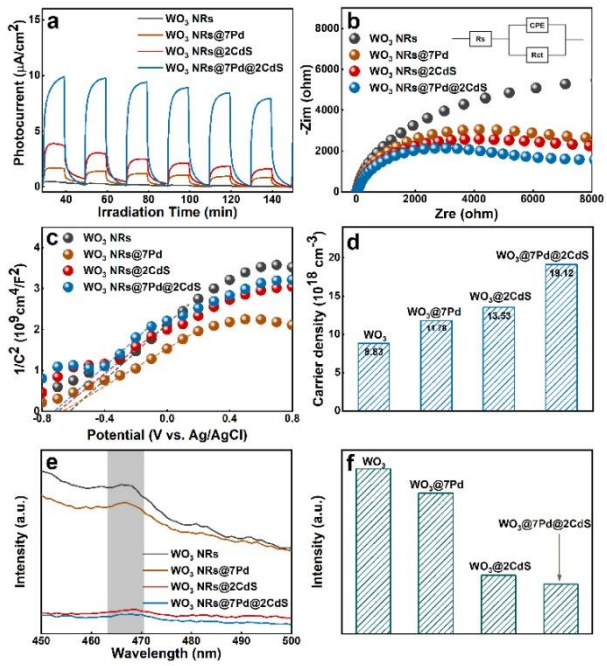

Fig. 7. (a) Photocurrent, (b) EIS Nyquist plots and (c) M–S results & (d) charge density (N_b) of WO_3 NRs, WO_3 NRs@7Pd, WO_3 NRs@2CdS and WO_3 NRs@7Pd@2CdS under the illumination of visible light (λ>420 nm) (Na_2SO_4: 0.5 M, pH=6.69); (e) PL spectra of different samples (λ_{Exc}=380 nm) and (f) peak intensity comparison.

transfer constitutes the photocatalytic mechanism of WO_3 NRs@Pd@CdS, for which electrons in the CB of WO_3 and holes in the VB of CdS rapidly recombine at the interface by way of Pd NCs, leaving electrons and holes with high redox capability to trigger the photoredox catalysis (**Fig. S20b)**.

As demonstrated in **Scheme 2**, once WO_3 NRs@Pd@CdS heterostructure is illuminated by visible light, WO_3 core and CdS shell are simultaneously photoexcited to yield the electron-hole pairs. Immediately, electrons in the CB of WO_3 flow to the Pd NCs which are integrated at the interface of WO_3 and CdS and then rapidly recombine with holes in the VB of CdS to trigger the Z-scheme charge transport, ultimately leaving electrons and holes with substantial redox capacity in the CB of CdS and VB of WO_3, respectively. In this way, Pd NCs serve as efficient Schottky-type electron flow mediators for promoted charge migration. Hence, subsequently, electrons in the CB of CdS are involved in photoreduction of nitroaromatics, wherein holes in the VB of WO_3 are completely quenched by ammonium formate under continuous N_2-bubbling and it ensures electrons the only active specie in photoreduction reaction. It should be emphasized that holes left in the VB of WO_3 NRs are beneficial for the generation of oxygen-containing active species (e.g., $•O^{2-}$ and •OH) to initiate the selective photocatalytic oxidation of BA to BAD. Redox potentials of BA and BAD are determined by CV analysis. As exhibited in **Fig. S21a**, CV curves indicate BA redox potential is not influenced by concentration and the first peak is assigned to the BA oxidation to BAD (+1.84 V vs. NHE) and the second peak suggests the BAD oxidation to acids, (+2.49 V vs. NHE). To evidence the speculation, CV results of BAD (**Fig. S21b)** is additionally explored and the result is consistent with the second BA oxidation peak. As a result, it is reasonably speculated that holes left in the VB of WO_3 are able to directly oxidize aromatic alcohols to aldehydes owing to the favorable energy level position. Regarding the selective aromatic alcohols oxidation to aldehydes (**Fig. S22**) under visible light illumination, alcohols are adsorbed on the WO_3 surface by deprotonation to generate structural-II and the adsorbed alcohols first react with holes and then deprotonate to form carbon radicals (structure-III). Considering the appropriate energy level positions, electrons in the CB of CdS can react with dissolved O_2 to generate superoxide ($•O^{2-}$) radicals, while holes in the VB of WO_3 oxidizes H_2O/−OH to •OH radicals. The $•O^{2-}$/•OH radicals are involved in selective aromatic alcohols oxidation to aldehydes and form intermediates IV with carbon radicals. The interaction between C-O and O-O bonds of alcohols synergistically produce hydrogen peroxide through the oxygen bridge structure, fulfilling the photocatalytic selective oxidation process.[26, 59]

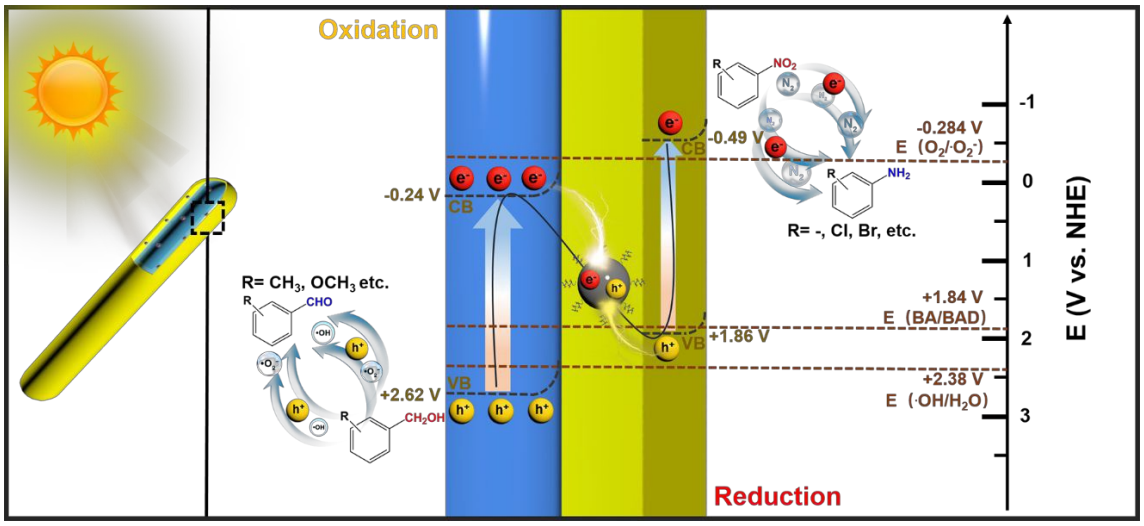

Scheme 2. Schematic diagram illustrating the photoredox mechanism of WO_3 NRs@Pd@CdS heterostructures.

Besides, holes in the VB of WO_3 can also take part in the direct aromatic alcohols oxidization to aldehydes.

4. Conclusions

In summary, Z-scheme artificial photosystem was elaborately designed on the WO_3 NRs with Pd NCs self-assembled on the surface followed by uniform CdS encapsulation leading to WO_3 NRs@Pd@CdS core-shell heterostructure. The WO_3 NRs@Pd@CdS heterostructure exhibits significantly enhanced net efficiency of photoactivities toward selective reduction of nitroaromatics to amino derivatives and selective oxidation of aromatic alcohols to aldehydes with favorable photostability. The Pd NCs integrated in-between WO_3 core and CdS shell considerably accelerate the Z-scheme charge transfer, wherein Pd NCs serve as high-efficiency Schottky-type electron transport mediators, giving rise to the considerably improved charge separation and greatly enhanced photoredox performances. Dominant active species in-situ formed in the photoredox organic transformation were identified with Z-scheme photoredox mechanism clearly elucidated. Our work demonstrates a promising and sustainable paradigm for smartly designing Z-scheme photosystems for solar-to-chemical energy conversion.

Conflicts of interest

There are no conflicts to declare.

Acknowledgements

The support by the award Program for Minjiang scholar professorship is greatly acknowledged. This work was financially supported by the National Natural Science Foundation of China (Nos. 21703038).

Notes and references

1 H. Wang, L. Zhang, Z. Chen, J. Hu, S. Li, Z. Wang, J. Liu and X. Wang, *Chem. Soc. Rev.*, 2014, **43**, 5234-5244.
2 F. Chen, H. Huang, L. Guo, Y. Zhang and T. Ma, *Angew. Chem. Int. Ed. Engl.*, 2019, **58**, 10061-10073.
3 W. Yu, S. Zhang, J. Chen, P. Xia, M. H. Richter, L. Chen, W. Xu, J. Jin, S. Chen and T. Peng, *J. Mater. Chem. A*, 2018, **6**, 15668-15674.
4 S. Hou, Z. Q. Wei, X. C. Dai, M. H. Huang and F. X. Xiao, *Inorg. Chem.*, 2020, **59**, 7325-7334.
5 H.-J. Lin, S. Xu, X.-Y. Fu, Z.-Q. Wei, M.-H. Huang, X. Lin, Y. He, G. Xiao and F.-X. Xiao, *Inorg. Chem.*, 2020, **59**, 4129-4139.
6 S. Liu, M. Q. Yang, Z. R. Tang and Y. J. Xu, *Nanoscale*, 2014, **6**, 7193-7198.
7 C. Liu, N. P. Dasgupta and P. Yang, *Chem. Mater.*, 2014, **26**, 415-422.
8 A. Dhakshinamoorthy, S. Navalon, A. Corma and H. Garcia, *Energy Environ. Sci.,* 2012, **5**. 9217-9233.
9 Y. H. Ng, S. Ikeda, M. Matsumura and R. Amal, *Energy Environ. Sci.,* 2012, **5**. 9307-9318.
10 Z. Zeng, Y.-B. Li, S. Chen, P. Chen and F.-X. Xiao, *J. Mater. Chem. A*, 2018, **6**, 11154-11162.
11 R. Abe, K. Sayama, K. Domen and H. Arakawa, *Chem. Phys. Lett.*, 2001, **344**, 339-344.
12 K. S. Leschkies, R. Divakar, J. Basu, E. Enache-Pommer, J. E. Boercker, C. B. Carter, U. R. Kortshagen, D. J. Norris and E. S. Aydil, *Nano Lett.*, 2007, **7**, 1793-1798.
13 D. B. Ingram and S. Linic, *J. Am. Chem. Soc.*, 2011, **133**, 5202-5205.
14 J. S. DuChene, B. C. Sweeny, A. C. Johnston-Peck, D. Su, E. A. Stach and W. D. Wei, *Angew. Chem. Int. Ed. Engl.*, 2014, **53**, 7887-7891.
15 H. J. Chen, L. Shao, Q. Li and J. F. Wang, *Chem. Soc. Rev.*, 2013, **42**, 2679-2724.
16 L. J. Zhang, S. Li, B. K. Liu, D. J. Wang and T. F. Xie, *ACS Catal.*, 2014, **4**, 3724-3729.
17 K.-Y. Jiang, X.-C. Dai, Y. Yu, Q.-L. Mo and F.-X. Xiao, *J. Phys. Chem. C,* 2018, **122**, 12291-12306.
18 Y.-B. Li, T. Li, X.-C. Dai, M.-H. Huang, Y. He, G. Xiao and F.-X. Xiao, *J. Mater. Chem. A*, 2019, **7**, 8938-8951.
19 W. Xiang, Y. Zhao, Z. Jiang, X. Li, H. Zhang, Y. Sun, Z. Ning, F. Du, P. Gao, J. Qian, K. Kato, M. Yamauchi and Y. Sun, *J. Mater. Chem. A*, 2018, **6**, 23366-23377.
20 Y. X. Pan, Y. You, S. Xin, Y. Li, G. Fu, Z. Cui, Y. L. Men, F. F. Cao, S. H. Yu and J. B. Goodenough, *J. Am. Chem. Soc.*, 2017, **139**, 4123-4129.
21 M.-H. Huang, Y.-B. Li, T. Li, X.-C. Dai, S. Hou, Y. He, G. Xiao and F.-X. Xiao, *Chem. Commun.*, 2019, **55**, 10591-10594.
22 M.-H. Huang, X.-C. Dai, T. Li, Y.-B. Li, Y. He, G. Xiao and F.-X. Xiao, *J. Phys. Chem. C,* 2019, **123**, 9721-9734.
23 H.-J. Lin, T. Li, M.-H. Huang, X.-C. Dai, Y.-B. Li and F.-X. Xiao, *J. Phys. Chem. C,* 2019, **123**, 28066-28080.
24 24. P. Zhou, J. Yu and M. Jaroniec, *Adv. Mater.*, 2014, **26**, 4920-4935.
25 Y. B. Li, T. Li, X. C. Dai, M. H. Huang, S. Hou, X. Y. Fu, Z. Q. Wei, Y. He, G. Xiao and F. X. Xiao, *ACS Appl Mater Interfaces*, 2020, **12**, 4373-4384.
26 S. Xu, M.-H. Huang, T. Li, Z.-Q. Wei, X. Lin, X.-C. Dai, S. Hou, X.-Y. Fu and F.-X. Xiao, *J. Mater. Chem. A*, 2020, **8**, 8360-8375.
27 M. Seifollahi Bazarjani, M. Hojamberdiev, K. Morita, G. Zhu, G. Cherkashinin, C. Fasel, T. Herrmann, H. Breitzke, A. Gurlo and R. Riedel, *J. Am. Chem. Soc.*, 2013, **135**, 4467-4475.
28 Y. Xiao, T. Wang, G. Qiu, K. Zhang, C. Xue and B. Li, *J. Colloid Interface Sci.*, 2020, **577**, 459-470.
29 Y. Xiao, X. Tao, G. Qiu, Z. Dai, P. Gao and B. Li, *J. Colloid Interface Sci.*, 2019, **550**, 99-109.
30 R. Wang, G. Qiu, Y. Xiao, X. Tao, W. Peng and B. Li, *J. Catal.*, 2019, **374**, 378-390.
31 X. Lin, Z.-Q. Wei, T. Li, M.-H. Huang, S. Xu, Y. He, G. Xiao and F.-X. Xiao, *Inorg. Chem.*, 2020, **59**, 1364-1375.
32 B. Weng, J. Wu, N. Zhang and Y. J. Xu, *Langmuir*, 2014, **30**, 5574-5584.
33 Z. R. Dai, J. P. Bradley, D. J. Joswiak, D. E. Brownlee, H. G. M. Hill and M. J. Genge, *Nature*, 2002, **418**, 157-159.
34 N. Zhang, S. Xie, B. Weng and Y.-J. Xu, *J. Mater. Chem. A*, 2016, **4**, 18804-18814.
35 H. Bader, V. Sturzenegger and J. Hoigné, *Water Res.*, 1988, **22**, 1109-1115.
36 F.-X. Xiao and B. Liu, *Adv. Mater. Interfaces*, 2018, **5**, 1701098.
37 Z.-Q. Wei, X.-C. Dai, S. Hou, Y.-B. Li, M.-H. Huang, T. Li, S. Xu and F.-X. Xiao, *J. Mater. Chem. A*, 2020, **8**, 177-189.
38 D. I. Gittins and F. Caruso, *Angew. Chem. Int. Edit.*, 2001, **40**, 3001-3004.
39 B. Gerand, G. Nowogrocki, J. Guenot and M. Figlarz, *J. Solid State Chem.*, 1979, **29**, 429-434.
40 T. Li, Y.-B. Li, X.-C. Dai, M.-H. Huang, Y. He, G. Xiao and F.-X. Xiao, *J. Phys. Chem. C,* 2019, **123**, 4701-4714.

View Article Online
DOI: 10.1039/D0TA07235D

41 P.-Y. Kuang, P.-X. Zheng, Z.-Q. Liu, J.-L. Lei, H. Wu, N. Li and T.-Y. Ma, *Small*, 2016, **12**, 6735-6744.
42 D. Chen and J. Ye, *Adv. Funct. Mater.*, 2008, **18**, 1922-1928.
43 43. Z.-Y. Liang, J.-X. Wei, X. Wang, Y. Yu and F.-X. Xiao, *J. Mater. Chem. A*, 2017, **5**, 15601-15612.
44 F. Xu, Y. Yao, D. Bai, R. Xu, J. Mei, D. Wu, Z. Gao and K. Jiang, *RSC Adv.*, 2015, **5**, 60339-60344.
45 X.-Y. Fu, Y.-B. Li, M.-H. Huang, T. Li, X.-C. Dai, S. Hou, Z.-Q. Wei and F.-X. Xiao, *Inorg. Chem.*, 2020, **59**, 2562-2574.
46 T. Li, M.-H. Huang, Y.-B. Li, X.-C. Dai, Y. He, G. Xiao and F.-X. Xiao, *J. Mater. Chem. A*, 2019, **7**, 21182-21194.
47 K. R. Priolkar, P. Bera, P. R. Sarode, M. S. Hegde, S. Emura, R. Kumashiro and N. P. Lalla, *Chem. Mater.*, 2002, **14**, 2120-2128.
48 R. A. Campbell, J. Rodriguez and D. W. Goodman, *Surf. Sci.*, 1990, **240**, 71-80.
49 R. Wang, B. Li, Y. Xiao, X. Tao, X. Su and X. Dong, *J. Catal.*, 2018, **364**, 154-165.
50 B. Li, L. Shao, R. Wang, X. Dong, F. Zhao, P. Gao and Z. Li, *J. Mater. Chem. A*, 2018, **6**, 6344-6355.
51 N. Zhang and Y.-J. Xu, *Chem. Mater.*, 2013, **25**, 1979-1988.
52 Z. R. Dai, J. P. Bradley, D. J. Joswiak, D. E. Brownlee, H. G. Hill and M. J. Genge, *Nature*, 2002, **418**, 157-159.
53 F. X. Xiao and B. Liu, *Nanoscale*, 2017, **9**, 17118-17132.
54 X.-C. Dai, M.-H. Huang, Y.-B. Li, T. Li, B.-B. Zhang, Y. He, G. Xiao and F.-X. Xiao, *J. Mater. Chem. A*, 2019, **7**, 2741-2753.
55 R. Ab Kadir, W. Zhang, Y. Wang, J. Z. Ou, W. Wlodarski, A. P. O'Mullane, G. Bryant, M. Taylor and K. Kalantar-zadeh, *J. Mater. Chem. A*, 2015, **3**, 7994-8001.
56 Y. H. Lee, X. Q. Zhang, W. Zhang, M. T. Chang, C. T. Lin, K. D. Chang, Y. C. Yu, J. T. Wang, C. S. Chang, L. J. Li and T. W. Lin, *Adv Mater*, 2012, **24**, 2320-2325.
57 J. Xiao, Y. Xie, C. Li, J.-H. Kim, K. Tang and H. Cao, *Catal. Today*, 2018, **307**, 147-153.
58 Z.-Y. Liang, M.-H. Huang, S.-Y. Guo, Y. Yu, W. Chen and F.-X. Xiao, *Catal. Sci. Technol.*, 2019, **9**, 672-687.
59 Y. Su, Z. Han, L. Zhang, W. Wang, M. Duan, X. Li, Y. Zheng, Y. Wang and X. Lei, *Appl. Catal. B*, 2017, **217**, 108-114

View Article Online
DOI: 10.1039/D0TA07235D

Table of Contents Graphic

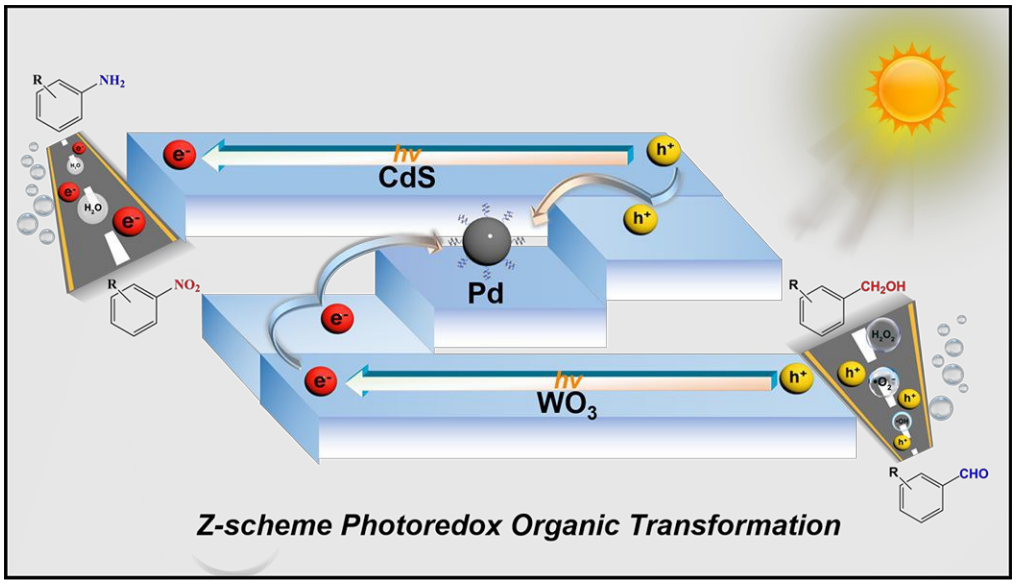

An all-solid-state Z-scheme photoredox system was elaborately designed over core-shell multilayered heterostructures for multifarious photoredox organic transformation under visible light.